



Improved Mars Helicopter Aerodynamic Rotor Model for Comprehensive Analyses

Witold J. F. Koning* and Wayne Johnson†

NASA Ames Research Center, Moffett Field, California 94035

and

Håvard F. Grip‡

California Institute of Technology, Pasadena, California 91109

DOI: 10.2514/1.J058045

The Mars Helicopter is part of the NASA Mars 2020 rover mission scheduled to launch in July of 2020. Its goal is to demonstrate the viability and potential of heavier-than-air vehicles in the Martian atmosphere. The low density of the Martian atmosphere and the relatively small-scale rotor result in flows with very low Reynolds number, reducing the lifting force and lifting efficiency, respectively. This paper describes the generation of the improved Mars Helicopter aerodynamic rotor model. The goal is to generate a performance model for the Mars Helicopter rotor using a free wake analysis in CAMRADII. The improvements in the analysis are twofold and are expanded on from two prior publications. First, the fidelity of the simulations is increased by performing higher-order time-accurate OVERFLOW simulations allowing for higher-accuracy aerodynamic coefficients and a better understanding of the boundary-layer behavior. Second, a model is generated for the testing conditions in the 25-ft-diam Space Simulator at the Jet Propulsion Laboratory, allowing for better correlation of rotor performance figures. The higher temperatures in the experiment are expected to give conservative performance estimates, as they give rise to an increase in speed of sound and decrease in observed Reynolds numbers.

Nomenclature

A	=	rotor disk area, m^2
a	=	speed of sound, m/s
C_P	=	rotor power coefficient, $P/(\rho A(\Omega R)^3)$
C_T	=	rotor thrust coefficient, $T/(\rho A(\Omega R)^2)$
c	=	airfoil chord, m
c_d	=	section drag coefficient, $D/(0.5\rho V^2 c)$
c_l	=	section lift coefficient, $L/(0.5\rho V^2 c)$
c_m	=	section pitch moment coefficient, $M_a/(0.5\rho V^2 c^2)$
D	=	section aerodynamic drag force, N/m
FM	=	hover figure of merit, $T\sqrt{T}/(2\rho A)/P$
g	=	gravitational acceleration, m/s^2
L	=	section aerodynamic lift force, N/m
M	=	blade section Mach number
M_a	=	section aerodynamic pitch moment, N
N	=	amplification factor
P	=	rotorcraft power, W
p	=	static pressure, kPa
R	=	gas constant, $m/(s^2 \cdot K)$; rotor radius, m
Re	=	Reynolds number
r	=	rotor radial coordinate, m
s	=	chordwise spacing, $\%c$
T	=	absolute temperature, K ; rotor thrust, N
t	=	airfoil thickness, m
V	=	section resultant velocity, m/s
y^+	=	dimensionless wall distance
α	=	angle of attack, deg

γ	=	specific heat ratio
μ	=	dynamic viscosity, $(N \cdot s)/m^2$
ρ	=	density, kg/m^3
σ	=	rotor solidity
Ω	=	rotor rotational speed, rad/s

Subscripts

c	=	chord-based
LE	=	leading edge
max	=	maximum
TE	=	trailing edge

I. Introduction

THE NASA Jet Propulsion Laboratory (JPL) designed the Mars Helicopter (MH) in collaboration with AeroVironment Inc., NASA Ames Research Center, and NASA Langley Research Center to explore the possibility of a vertical take-off and landing (VTOL) unmanned aerial vehicle (UAV) for flight on Mars. The helicopter joins the NASA Mars 2020 mission, currently scheduled to launch in July of 2020, to demonstrate the viability and potential of heavier-than-air vehicles in the Martian atmosphere.

Development started late 2013, and Balam and Tokumaru published the initial conceptual design of the current MH in 2014 [1]. Grip et al. more recently published a paper describing the flight dynamics of the MH and experimental testing in the 25-ft-diam Space Simulator (SS) at JPL [2]. Balam et al. described the full-scale technology demonstrator [3]. Koning et al. published performance predictions for the MH rotor and also evaluated the feasibility of cambered plates as substitute airfoils for the rotor [4,5].

The helicopter is mounted on the bottom of the Mars 2020 rover for its journey to Mars. The rover places the helicopter on the ground after touchdown, starting a 30-day flight test campaign of up to five flights of a few hundred meters. The present work describes the second generation of the performance model for the MH rotor using a free wake analysis.

Mars Helicopter Design: The design of the MH, shown in Fig. 1, features a co-axial rotor with a mass of roughly 1.8 kg and a 1.21 m rotor diameter. The helicopter relies on solar cells and a battery system for power, allowing up to 90 s flight endurance that is

Presented at the 44th European Rotorcraft Forum, Delft, The Netherlands, September 18–21, 2018; received 25 October 2018; revision received 17 April 2019; accepted for publication 7 June 2019; published online 3 July 2019. This material is declared a work of the U.S. Government and is not subject to copyright protection in the United States. All requests for copying and permission to reprint should be submitted to CCC at www.copyright.com; employ the eISSN 1533-385X to initiate your request. See also AIAA Rights and Permissions www.aiaa.org/randp.

*Aerospace Engineer, Aeromechanics Branch, and Science and Technology Corporation; witold.koning@nasa.gov. Member AIAA.

†Aerospace Engineer, Aeromechanics Branch; wayne.johnson@nasa.gov. Fellow AIAA.

‡Mars Helicopter GNC and Aerodynamics Lead, Robotics Technologist, JPL Guidance and Control Section, Jet Propulsion Laboratory; havard.f.grip@jpl.nasa.gov.

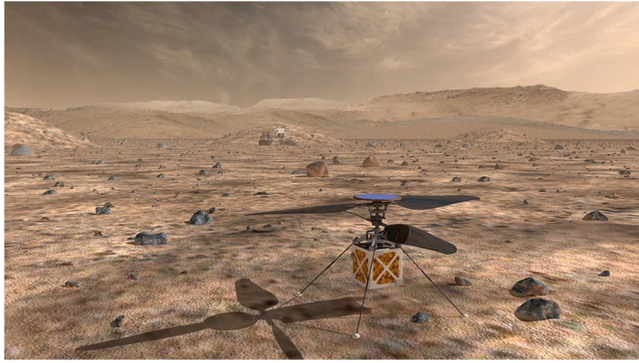


Fig. 1 An artistic depiction of the Mars Helicopter [6].

conducted fully autonomously due to the communication delay between Earth and Mars.

The rotor design features two counterrotating, hingeless, two-bladed rotors. The rotors are spaced apart at approximately 8–9% of the rotor diameter and are designed to operate at speeds up to 2800 RPM. The tip speed and tip Mach number during hover in the Martian atmosphere are roughly $V_{tip} = 177$ m/s and $M_{tip} = 0.76$, respectively. Flights are limited to favorable weather with low wind and gust speeds. The maximum airspeed is constrained to 10 m/s horizontally and 3 m/s vertically [2].

II. Mars Atmospheric Conditions

The Martian environment provides major challenges for the design of a UAV. The low density of the Martian atmosphere and the relatively small MH rotor result in very low chord-based Reynolds number flows with a range of $Re_c \approx 10^3$ to 10^4 (see Fig. 2).

The low density and low Reynolds number reduce the lift force and lift efficiency, respectively, which are only marginally compensated by a lower gravitational acceleration of around $g = 3.71$ m/s². In addition, the low-temperature and largely CO₂-based atmosphere results in a low speed of sound, further constraining rotor operation in the Martian atmosphere. Young et al. present the possibilities and limitations of Mars rotorcraft [7,8] and also indicate the potential of cambered plates for airfoils [9]. Escobar et al. describe the complexities in developing a coaxial Mars rotorcraft [10].

III. Low-Reynolds-Number Aerodynamics

The very low chord-based Reynolds numbers of the MH rotor, around $Re_c \approx 10^4$, result in relatively poor lift-to-drag ratios when compared with conventional performance figures at higher Reynolds numbers. At these low Reynolds numbers, starting below approximately $Re_c \approx 10^5$, the boundary-layer state can be subcritical. The term *critical* is used here to indicate the termination of low drag and commencement of laminar separation from a streamlined shape [11]. The flow is only called subcritical if the boundary-layer flow is laminar for the range of angles of attack. The corresponding Reynolds number at which the boundary layer just begins to exhibit turbulent features is the critical Reynolds number.

McMasters and Henderson provide an overview of experimental airfoil performance over a wide Reynolds number spectrum [12].

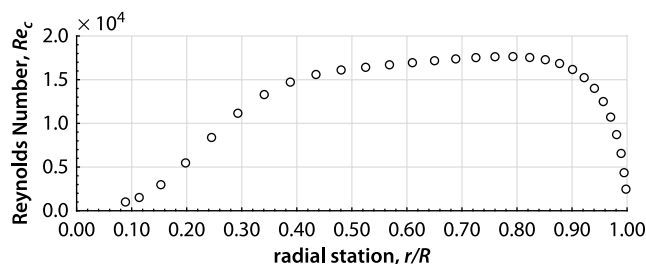


Fig. 2 Approximate spanwise Reynolds number distribution for the MH rotor in the Martian atmosphere, from Koning et al. [4].

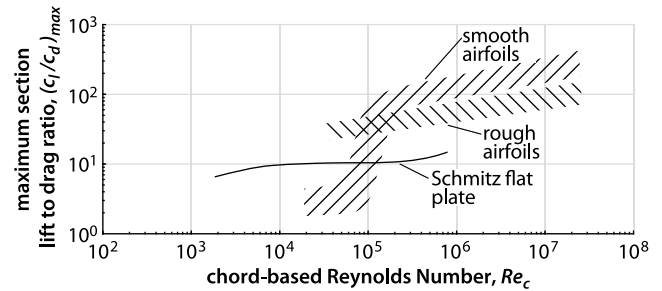


Fig. 3 Maximum section lift-to-drag ratio versus Reynolds number, from McMasters and Henderson [12].

Figure 3 shows the maximum section lift-to-drag ratio versus Reynolds number. The aforementioned performance drop is visible around approximately $Re_c \approx 10^5$. Rough airfoils exhibit higher performance down to slightly lower Reynolds numbers, because of the roughness contribution to boundary-layer transition.

The dramatic performance drop at low Reynolds numbers is primarily attributed to the rise in drag coefficient in the critical Reynolds number range. This is illustrated by the minimum section drag coefficient versus Reynolds number shown in Fig. 4. The low performance figures clearly indicate the need for careful design and evaluation of airfoils and rotors to be used in the low-Reynolds-number regime.

A. Subcritical Airfoil Performance

In the low-Reynolds-number regime, the boundary layer can still be laminar after the point of pressure recovery. The laminar boundary layer at lower Reynolds numbers does not encounter sufficient amplification of disturbances in time to experience on-body transition or turbulent flow reattachment after laminar separation. The laminar boundary layer carries much less momentum near the surface due to the absence of the momentum exchanges found in a typical turbulent boundary layer, and therefore cannot withstand a strong adverse pressure gradient without separating. Separation of the laminar boundary layer then gives rise to a large pressure drag component. Furthermore, the relatively thick boundary layer at low Reynolds numbers reduces the effective camber of the airfoil, reducing the attainable lift coefficient, especially if a separated shear layer fails to reattach.

The turbulent boundary layer exhibits higher resultant losses and friction drag compared with laminar boundary layer. However, the turbulent layer has higher near-wall velocity and momentum that allows for larger positive pressures (due to an adverse pressure gradient) before separation, resulting in higher airfoil performance of airfoils in supercritical states.

1. Mars Helicopter Boundary-Layer State Analysis

Koning et al. performed an evaluation of the two-dimensional boundary-layer state for the MH airfoils in hover [4]. The analyses were performed solely to obtain the boundary-layer state, and not to estimate aerodynamic coefficients.

The instability and laminar separation locations were computed from the momentum-integral equation derived from the work of

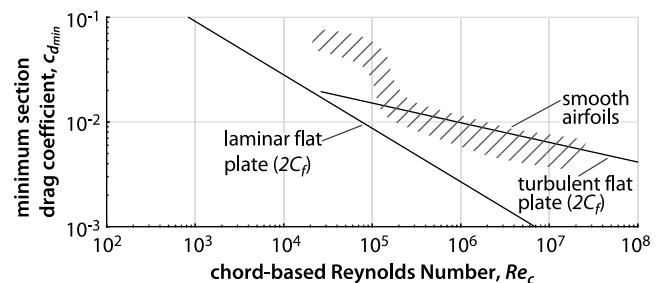


Fig. 4 Minimum section drag coefficient versus Reynolds number, from McMasters and Henderson [12].

Schlichting and Kestin [13] and Wazzan et al. [14]. A Karman-Tsien compressibility correction [15] was performed on the potential flow velocity distribution to account for first-order compressibility effects. Tollmien–Schlichting (TS) waves were assumed to be the dominant transition-initiation mechanism and were computed using the method suggested by Smith and Gamberoni [16] using stability charts from Wazzan et al. [14]. The airfoils were then analyzed for the expected angles of attack and Mach numbers at various radial stations for the rotor in hover. The analysis allowed for the computation of disturbance growth over the airfoils and estimation of transition, analogous to the e^N method, based on linear stability theory by van Ingen [17].

The maximum amplification factor was computed over the contour length, and the largest total amplification factor at the point of laminar separation was estimated. For the majority of the radial locations evaluated, the first most amplified frequency results in an amplification factor $N \leq 1$, not exceeding $N \approx 2$ at laminar separation. The likelihood of boundary-layer transition to turbulence at any airfoil station is deduced to be very low for the rotor in hover.

The method computes the amplitude ratio and not the actual disturbance amplitude because external influences are not known. Freestream turbulence levels, vibrations, dust, or surface roughness can all add to the actual disturbance amplitude. However, evaluating the former is complicated due to the importance of the distribution across the frequency spectrum, besides the freestream turbulence level [18]. This is difficult to predict and model and is therefore not attempted. Freestream turbulence levels might be very low in the free atmosphere, but the lower rotor might experience increased turbulence levels from the upper rotor wake. Vibrations and dust require higher knowledge of the rotor system and atmospheric dust behavior in the Martian atmosphere, work that is currently being pursued⁸. It is concluded that flow conditions would have to be severe to cause transition of the boundary layer before laminar separation of the boundary layer.

Lissaman observes that complete laminar flow can occur for small angles of attack below $Re_c \approx 3.0 \cdot 10^4$ with boundary-layer reattachment unlikely below $Re_c \approx 7.0 \cdot 10^4$ [19]. The absence of transition has also been observed by Mueller and DeLaurier [20] who state, after Carmichael [21], that for airfoils below $Re_c \approx 5.0 \cdot 10^4$ the free shear layer after laminar separation does not normally transition to turbulent flow in time to reattach to the airfoil surface.

The two-dimensional boundary-layer equations represent only an approximation of the true three-dimensional flowfield, even though the aspect ratio of the rotor blades should warrant the use of blade element models. The standard boundary-layer equations also assume thin boundary layers, which at increasingly lower Reynolds numbers become invalid. A higher-order boundary-layer formulation for airfoil performance evaluation, for example, that presented by Drela [22], would therefore be instrumental in future airfoil design optimization at very low Reynolds numbers.

The approach is also limited in evaluating compressibility features. A turbulence transition model is helpful to assess these features without assuming “fully turbulent” or fully laminar simulations.

2. Laminar Separation Bubbles and Shear-Layer Instability

The laminar separated shear layer is susceptible to transition and can undergo rapid transition to turbulent flow. The increased entrainment by the separated shear layer can lead to reattachment of the flow, creating a laminar separation bubble (LSB) [22–24]. The low velocities inside the bubble are linked to the characteristic flat pressure distribution of an LSB.

Periodic unsteadiness can be observed due to the unstable reattachment region caused by fluctuating entrainment of the fluid in the shear layer, periodic stabilization of the reverse-flow boundary layer, and possible developing eddy structures [25]. Movement of the bubble over the airfoil can therefore occur, as observed by Gaster [26].

⁸Work in progress on experimental dust studies and two-dimensional airfoil testing for low Reynolds numbers at NASA Ames Research Center.

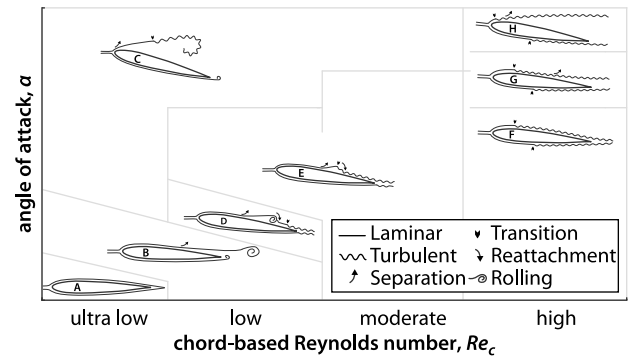


Fig. 5 Schematic of flow structures around NACA 0012 airfoil for each Reynolds number regime, from Wang et al. [29].

In addition to TS instabilities, the shear-layer flow is also observed to oscillate due to Kelvin–Helmholtz (KH) instabilities [25], which could develop into KH vortices if the flow does not reattach, thus causing fluctuating forces on the airfoil [23]. At high-subsonic Mach numbers, possible shock-induced separation and/or transition may cause additional complexities in the flow.

If an LSB occurs at the low Reynolds number, the level of freestream turbulence intensity can alter when, or if, reattachment occurs, and as such can strongly affect expected airfoil performance [27]. Angle of attack changes and boundary-layer receptivity, the process by which free-stream disturbances influence or generate instabilities in the boundary layer, can greatly influence bubble formation [28] and thus airfoil performance [29]. This is linked to the often significant hysteresis encountered in experimental low-Reynolds-number research around $Re_c \approx 10^5$ [11,28].

3. Low-Reynolds-Number Flow Structures

Wang et al. [29] and Huang and Lin [30] investigated flow structures and characteristics of vortex shedding for an NACA 0012 airfoil. Eight distinct flow patterns are identified based on angle of attack and Reynolds number. Figure 5 illustrates the different flow structures and stall modes for the NACA 0012 airfoil, showing more modes than the typical leading edge stall, trailing edge stall, and thin-airfoil stall known for higher-Reynolds-number regimes [31,32].

The different flow modes in Fig. 5 indicate the characteristic differences observed in the low-Reynolds-number regime. Flow structures B, “partially attached laminar boundary layer which separates near the trailing edge and then rolls up and/or experiences transition further downstream”; C, “fully separated laminar shear layer near the leading edge with a subsequent transition downstream but without reattachment”; and D, “laminar bubble, i.e., laminar flow from separation to reattachment” are some of the flow structures observed only for the low-Reynolds-number regime [29]. Flow mode D in particular indicates the necessity for time-accurate evaluation of the boundary layer in order to be able to investigate the flow structure and behavior adequately.

A thorough investigation on vortex shedding at low Reynolds numbers was performed by Yarusevych et al. [33]. The boundary-layer investigation on the MH rotor in hover predicts flow structure B to be dominant in the linear regime.

B. Cambered Plate Performance

Flat and cambered plates, especially with sharp leading edges, behave differently at low Reynolds numbers than conventional airfoils. The plate performance evaluation by Koning et al. [5] observed different flow structures from those found experimentally for smooth shapes at low Reynolds numbers by Wang et al. [29] (see Fig. 5). This is due to the vastly different geometry of the airfoils and resulting transient flow structures. Hoerner presents insight into differences in performance between a flat plate and an airfoil crossing the critical-Reynolds-number transition region [11]. The section lift and drag coefficient behavior near the critical Reynolds number are shown in Figs. 6 and 7, respectively.

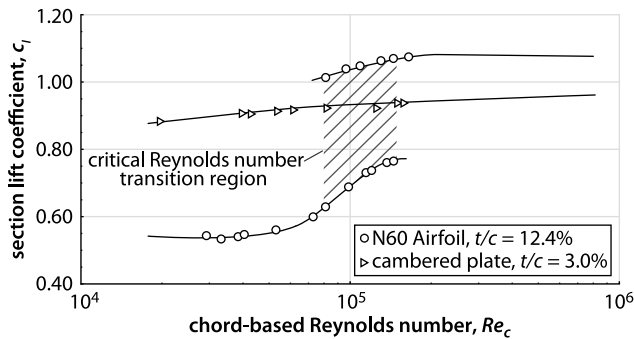


Fig. 6 Variation of section lift coefficient with Reynolds number at constant angle of attack, from Hoerner [11].

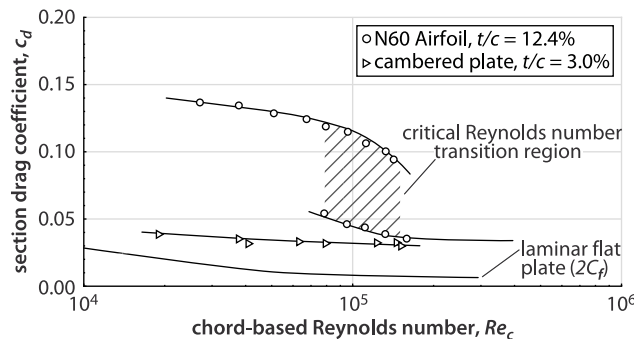


Fig. 7 Variation of section drag coefficient with Reynolds number at constant angle of attack, from Hoerner [11].

The cambered plates in the comparison have a thickness ratio of $t/c = 3.0\%$. The low thickness ratio has a beneficial effect on the drag coefficient [34,35].

The sharper the leading edge, the earlier transition starts [36]. For all positive angles of attack, the stagnation point moves downstream on the lower surface, creating a turbulent edge, essentially forcing supercritical behavior up to very low Reynolds numbers. A sharp leading edge plate therefore does not exhibit a critical Reynolds number because the point of breakaway is fixed. The turbulent edge has both an immediate and a fixed transition location at all nonzero angles of attack [36]. Crompton indicates the high shear turbulent fluid feedback and natural KH instability as main reasons for rapid transition [25]. He finds the transition to turbulence to be located at $x/c \approx 2.5\%$ for flat plates at $Re_c \approx 10^4$ – 10^5 [25]. Schmitz [36] notes that beneficial turbulent reattachment occurs for plates up to angles of attack around $\alpha \approx 7^\circ$ to 10° , whereas Crompton indicates reattachment up to $\alpha \approx 5^\circ$. Laitone [27] reports a similar range and observed for $Re_c < 4.0 \cdot 10^4$ and $\alpha < 8^\circ$ that the large leading edge bubble (compared with blunt leading edges) is replaced by continuous shedding of small vortices over the upper surface, thereby mitigating the effects of total flow separation.

Neither the trailing edge shape [27,37] nor freestream turbulence levels [37] seem to impact cambered or flat plate performance to any significance within the evaluated low-Reynolds-number range. No hysteresis occurs for thin plates, compared with that observed for thicker airfoils, because the nose turbulence increases faster than the pressure increase [36]. Okamoto et al. [35], Laitone [27], and Pelletier and Mueller [37] show the comparatively low influence of freestream turbulence.

However, a Reynolds number must exist at which the boundary layer does not transition to turbulence, despite the sharp leading edge. Indeed, flat plates at low Reynolds numbers around $Re_c \approx 10^4$ have been shown to have laminar flows without transition to turbulence [38,39].

Experimental results seem to contradict each other on whether turbulent reattachment of the separated shear layer on the leading edge of a flat plate indeed occurs. Laitone [27] does not mention an LSB, and Pelletier and Mueller [37] do not observe an LSB for

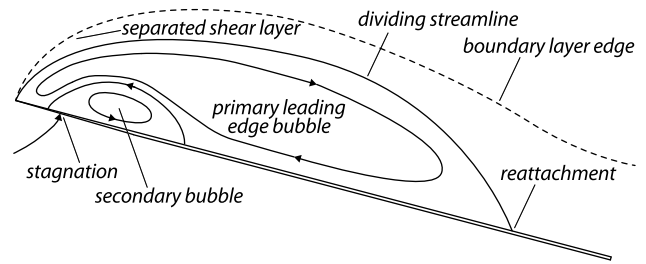


Fig. 8 Sketch of leading edge separation bubble on a flat plate with sharp leading edge (not to scale), from Sampaio et al. [43].

(cambered) flat plates and airfoils around $Re_c \approx 10^4$. In the experimental work by Suwa et al. [40] and Anyoji et al. [41,42], however, the existence of an LSB is deduced from the pressure distribution obtained via pressure sensitive paint observations for similar geometry and Reynolds numbers. Anyoji et al. find the flat plate reattachment state to disappear between $Re_c \approx 4.3 \cdot 10^3$ and $1.1 \cdot 10^4$ [41]. It is unclear to what extent the evaluation of the flow field using time-accurate and time-averaged methods might skew observations of the existence of an LSB.

Schmitz says $Re_c \approx 1.0 \cdot 10^4$ to $2.0 \cdot 10^4$ is enough for sharp leading edge boundary-layer transition [36]. Werlé shows a flat plate at $\alpha \approx 2.5^\circ$ and $Re_c \approx 1.0 \cdot 10^4$ with laminar reattachment, whereas at $Re_c \approx 5.0 \cdot 10^4$ the shear layer turns turbulent before reattachment [38,39].

Using direct numerical simulation (DNS), Sampaio et al. [43] show the possibility of a secondary separation bubble. This bubble was also observed by Crompton [25] experimentally. A sketch of the separation bubble on a flat plate is provided in Fig. 8. When the reattachment point reaches the trailing edge, the bubble effectively “bursts,” which is likely to generate periodic vortex shedding [36,44]. Wang et al. [29] observe that Gaster’s bursting criterion [26] for separation bubbles does not hold in the low-Reynolds-number regime.

Koning et al. show that the addition of camber to a sharp leading edge plate can indeed have very competitive performance to the airfoils discussed in the present research [5]. Unsteady Reynolds-averaged Navier–Stokes (URANS) computations showed both leading edge bubbles and transient upper surface vortex shedding that decreased the separated flow. This is attributed to the leading edge geometry as also experimentally observed by Laitone [27]. At smaller angles of attack, the flow seems to reach a steady state by means of a separation bubble similar to that reported by Suwa et al. [40], Anyoji et al. [41,42], and others.

The Reynolds number sensitivities of the flat plate minimum drag coefficient and maximum lift-to-drag ratio were in agreement with the results of Schmitz [36] and two-dimensional laminar flat plate theory. The cambered plate was observed to obtain a higher lift-to-drag ratio than the flat plate, despite the unavoidable increase in minimum section drag.

IV. Prior Rotor Performance Predictions

Figure 9 shows the performance predictions from Koning et al. for figure of merit versus blade loading [4]. Performance is calculated by comprehensive analysis in CAMRADII using a free wake geometry, and airfoil tables are generated by computational fluid dynamics (CFD). The three conditions in Fig. 9 span expected operating conditions on Mars due to the change in atmosphere with diurnal cycles, and temperature varies along with density. The present analysis is performed only for Mars condition (MC) 2, as observed performance variation before peak figure of merit is minimal.

The predictions show generally good agreement with experimental results from the 25-ft-diam Space Simulator at JPL. However, the CFD analysis was performed using a thin-layer Navier–Stokes (NS) code and the measured data in Fig. 9 obtained at much higher temperature, leading to the need for a better CFD method and calculations performed at the correct temperature for proper comparison with measurements.

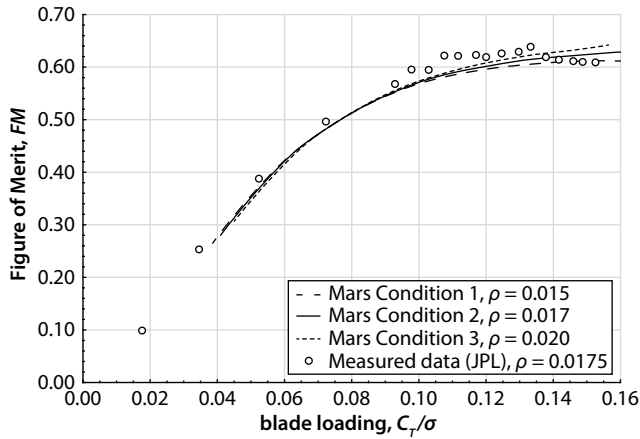


Fig. 9 Figure of merit versus blade loading for all Martian conditions, from Koning et al. [4].

Prediction improvements: Compared with the previous work by Koning et al. [4], the rotor model predictions in the present work have been improved on a couple of fronts. First, higher-fidelity, time-accurate simulations are employed in OVERFLOW to allow for higher-accuracy aerodynamic coefficients and better understanding of the flow structure. Second, airfoil geometries are redefined to allow for denser meshes, and trailing edge thickness is adjusted to reflect a realistic thickness. Third, a rotor model is made separately for the JPL experimental conditions and MC 2.

The main difference between JPL SS conditions and MC 2 is the operational temperature in the JPL SS experiments, as shown in Table 1. This causes roughly a 13% decrease in Mach number and 29% decrease in Reynolds number (due to the temperature dependence of the viscosity for CO_2) compared with Mars atmospheric conditions. It is estimated that this results in conservative experimental performance numbers from the JPL SS test conditions.

V. Computational Approach

Two-dimensional airfoil sections are analyzed using two-dimensional structured grids and solved using the implicit compressible RANS solver OVERFLOW 2.2n [45]. All solutions presented are run time-accurate, in an effort to quantify possible unsteady behavior, and use sixth-order central differencing of Euler terms with second-order BDF2 time marching [46]. In total, over 6000 simulations are performed on the Pleiades Supercomputer at NASA Ames Research Center.

A. Operating Conditions

Airfoil performance is evaluated for average Martian atmospheric conditions, MC 2, as previous work shows marginal performance differences with other variations [4]. Operating conditions for MC 2 are presented in Table 1 and compared with Earth sea-level standard (SLS) conditions.

Experiments in the 25-ft-diam Space Simulator at JPL are performed using CO_2 at similar gas density but at a different temperature range. The gas density is slightly different from that

reported in Fig. 9 for JPL measurements at later tests, to which the present models are compared, operated at a slightly higher gas density. The temperature in the JPL SS varied between $T = 293.15$ and 303.15 K during testing. The average temperature was used from the JPL SS operating conditions, and the corresponding viscosity obtained from Sutherland's equation with Sutherland's constants for CO_2 .

Free-stream turbulence and boundary-layer receptivity are generally important, but no further information is known. Therefore, the free-stream turbulence intensity (TI) is kept at the standard value $\text{TI} \approx 0.082\%$.

However, Wang et al. [29] experimentally show that the influence of the turbulence intensity is greatly diminished when the Reynolds number regime is low ($Re_c \approx 1.0 \cdot 10^4$ to $3.0 \cdot 10^5$) compared with the ultra-low regime ($Re_c < 1.0 \cdot 10^4$) [29].

Compressibility effects are expected to be small as shown by experimental work by Suwa et al. [40] and Anyoji et al. [41] for similar Mach-Reynolds number ranges. The (turbulent) Prandtl number is assumed to stay the same as for air.

The model is presented through airfoil data tables (C81 files) that are used by comprehensive rotor analysis codes. The angle of attack and Mach number range for each radial station are presented in Table 2. The angle of attack range uses 1 deg increments, and the Mach range uses increments equal to $M = 0.1$. Each radial station's (M, α) pair provides the lift, drag, and moment coefficients for the C81 airfoil deck files required for comprehensive analyses. The normalized airfoil profiles for the MH rotor are found in Koning et al. [4].

B. Turbulence and Transition Modeling

The previous rotor models [4] were generated using the Spalart-Allmaras (SA) 1-equation turbulence model [47] (SA-noft2) in "fully turbulent" mode. In the linear angle of attack range, the performance was found to be close to cases run fully laminar.

Transition modeling is realized using the SA 1-equation turbulence model (SA-neg-1a) with the Coder 2-equation Amplification Factor Transport (AFT) transition model (SA-AFT2017b) [48]. The SA-AFT2017b model is referred to as the "transition model" from here on out. This allows for a direct comparison to the flat plate model presented by Koning et al. [5], which uses the same turbulence and transition models.

The intermittency is deduced from the transport of the amplification factor in the flow. This allows for a comparison with the initial estimates of the amplification factor in the boundary layer (BL) of the initial MH rotor model [4]. The general understanding of the MH airfoil performance and flow conditions can therefore be improved.

The initial model deduced the BL state from a two-dimensional BL analysis. Limitations include a crude compressibility evaluation and simple empirical evaluation of the shear-layer behavior after separation. The transition model allows for a more thorough evaluation of these features and estimation of their effect on airfoil performance.

The evaluation of the upper rotor wake influence on transition locations of the lower rotor BL is not attempted due to the complexity of the problem. A three-dimensional model can provide more insight into the influence of upper rotor wake on lower rotor transition and perhaps quantify performance trends.

Table 1 Operating conditions for Mars condition 2 [4]

Variable	Earth SLS	MC 2	JPL SS
Density, ρ [kg/m^3]	1.225	0.017	0.0185
Temperature, T [K]	288.20	223.20	298.15
Gas constant, R [$\text{m}^2/(\text{s}^2 \cdot \text{K})$]	287.10	188.90	188.90
Specific heat ratio, γ	1.400	1.289	1.289
Dynamic viscosity, μ [$(\text{N} \cdot \text{s})/\text{m}^2$]	$1.750 \cdot 10^{-5}$	$1.130 \cdot 10^{-5}$	$1.504 \cdot 10^{-5}$
Static pressure, p [kPa]	101.30	0.72	1.04
Speed of sound, a [m/s]	340.35	233.13	269.44

Table 2 C81 alpha-Mach pair input parameters (MC 2)

CFD station	r/R	A , deg	M	Re/M , 10^{-4}
Station 1	0.091	−15 to 20	0.10 to 0.30	1.074
Station 2	0.200	−15 to 20	0.10 to 0.40	2.984
Station 3	0.295	−15 to 20	0.10 to 0.50	4.176
Station 4	0.390	−15 to 20	0.10 to 0.50	4.176
Station 5	0.527	−15 to 20	0.20 to 0.50	3.451
Station 6	0.762	−15 to 20	0.20 to 0.70	2.564
Station 7	0.924	−15 to 20	0.20 to 0.85	1.825
Station 8	0.991	−15 to 20	0.20 to 0.90	0.724

C. Time-Accurate Solver

The time-accurate solver allows for extraction of flow solutions over time and investigation of potential transient features for a better understanding of the flow, as was done by Koning et al. [5]. A script detects whether the converged integrated forces over the airfoil are periodic, and subsequently takes the mean and standard deviation over whole periods to ensure adequate averaging of the aerodynamic coefficients.

D. Geometry Definition and Grid Resolution Study

The clif5605 airfoil is used for a grid resolution study (GRS). The GRS is performed for two limiting cases: the highest and lowest Reynolds number expected at $r/R = 0.75$. The gridding guidelines from the third American Institute of Aeronautics and Astronautics (AIAA) CFD High Lift Prediction Workshop are used to generate different grids in four levels: coarse, medium, fine, and extra-fine [49]. A super-fine grid level is added.

The chordwise spacing at the leading edge (LE), s_{LE} , and trailing edge (TE), s_{TE} , are varied between 1 and $0.001c$. The maximum chordwise spacing, s_{max} , is limited between 0.5 and $1.0\%c$. The y^+ values are calculated for the first point off the airfoil surface at $10\%c$. The initial wall spacing layer contains five layers of constant cell spacing normal to the viscous walls. The cell stretching ratio (SR) for the normal and tangential/chordwise layers is kept identical and the farfield is located at $100c$ for all grids. The number of cells normal to the surface is obtained from the target stretching ratios. The number of cells over the trailing edge is monitored to ensure adequate gridding near the TE.

All grids are generated using Chimera Grid Tools (CGT) 2.3 [50]. The original airfoil contained a sharp trailing edge that resulted in unrealistically thin TEs. The airfoils have been adapted to use a $0.25\%c$ -thick rounded TE. An O-grid is preferred over a C-grid to remove the inherent bias in the wake resolution present in the latter.

The extra-fine grid level is ultimately chosen because it is the first level at which the section drag coefficients are converged up to the fourth decimal point. This is deemed sufficient as the C81 airfoil format only allows four decimal numbers for the aerodynamic coefficients.

E. Three-Dimensional Effects

All simulations performed are two-dimensional. The vast separation at moderate to high angles of attack can yield three-dimensional breakdown of the flow around $\alpha \approx 8^\circ$ [27,41,51]. Because the majority of the rotor is expected to operate in the linear regime, this is not pursued further at this time. With transition of the BL to turbulence unlikely in the design thrust coefficient range, cross-flow transition is assumed not to be critical for rotor performance and is not further evaluated.

VI. Simulation Results: Transition Model Influence

Sample airfoil performance results are presented for three outboard stations as section lift and section drag coefficient versus angle of attack in Figs. 10 and 11, respectively. The Mach numbers for the radial stations correspond to the hover Mach number at 2800 RPM, rounded to the closest available Mach number in the rotor deck (as summarized in Table 2).

Select airfoil stations are studied to investigate the flow structures simulated. Figure 12 shows the velocity field around station 6 with a laminar BL separating at the end of the airfoil. Outboard of station 5 ($r/R > 0.53$) the airfoils of the MH rotor are equal [4] and all flowfields presented are simulated at MC 2 conditions.

A. Transition Model Influence on Amplification Factor in Hover

The amplification factor is monitored for expected angle of attack and Mach combinations over the radial stations as published in Koning et al. [4]. In agreement with this paper, the amplification factor before laminar separation rarely exceeds $N = 1$. Figure 13 shows the amplification factor plot for station 7 at $\alpha = 3.00^\circ$, $M = 0.60$.

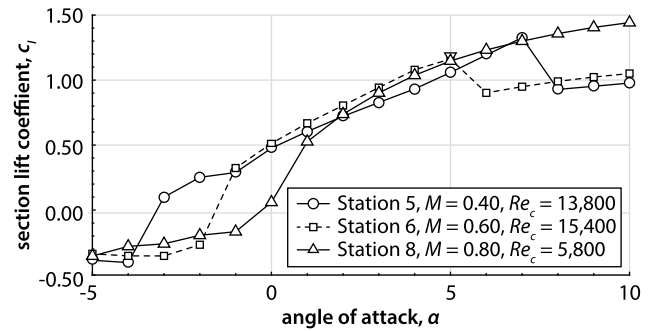


Fig. 10 Section lift coefficient versus angle of attack for stations 5, 6, and 8 at expected Mach and Reynolds numbers in hover.

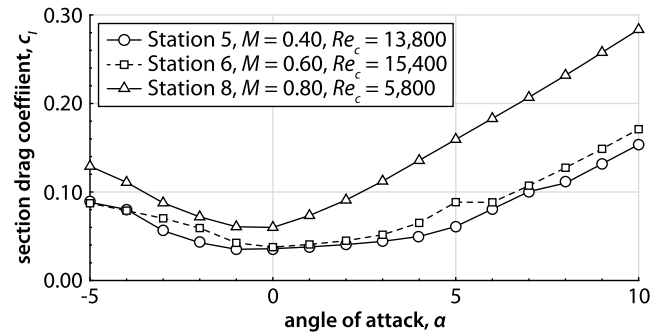


Fig. 11 Section drag coefficient versus angle of attack for stations 5, 6, and 8 at expected Mach and Reynolds numbers in hover.



Fig. 12 Laminar boundary layer with trailing edge separation and vortex shedding at $r/R = 0.76$, $\alpha = 0.00^\circ$, $M = 0.50$ (velocity magnitude, time-accurate, with transition model).

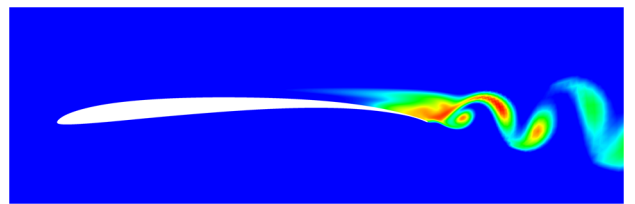


Fig. 13 Computed amplification factor in the flow at $r/R = 0.92$, $\alpha = 3.00^\circ$, $M = 0.60$. Values of $N < 1$ are solid blue (red is $N \approx 7$, time-accurate, with transition model).

The analysis by Koning et al. [4] does not evaluate the amplification factor after laminar separation. The present results agree with the analysis from Koning et al. up until laminar separation and also indicate that transition is unlikely in hover for the MH.

B. Transition Model Influence on Turbulence Behavior Near Stall

The SA turbulence model (SA-nof2) is run “fully turbulent,” meaning that production terms are active, without a trip line or a form of transition control. Koning et al. found that the turbulence model produces near-identical results to a fully laminar solution in the linear angle of attack range [4]. At higher angles of attack and higher Mach numbers, however, the model produces some turbulent features leading to higher performance than that of the laminar solution, even at the low Reynolds numbers under investigation. The transition

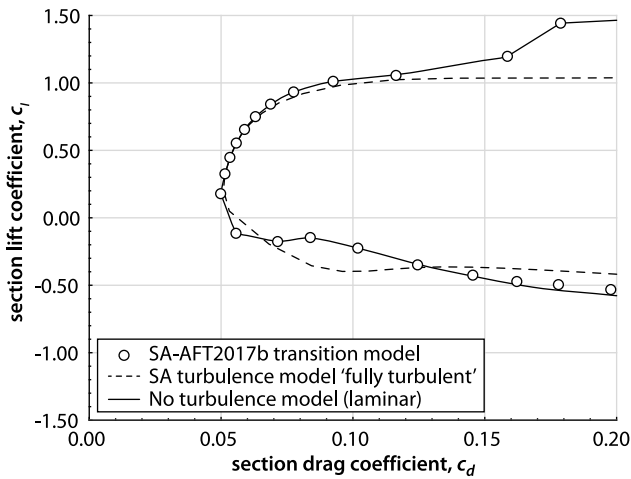


Fig. 14 Drag polars for laminar, “fully turbulent” SA turbulence, and SA-AFT2017b transition model, $r/R = 0.76$, $M = 0.20$.

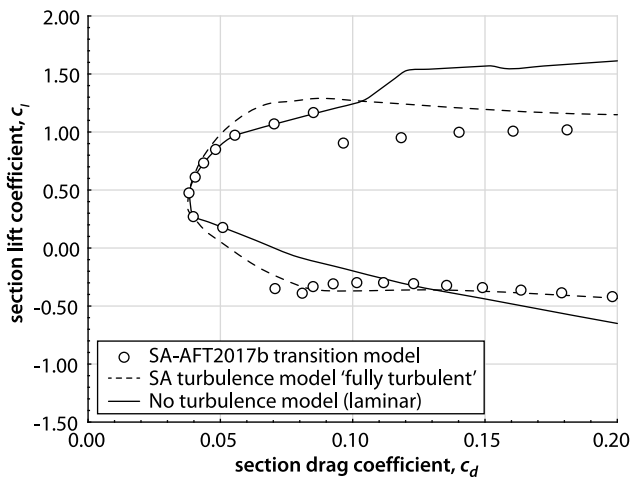


Fig. 15 Drag polars for laminar, “fully turbulent” SA turbulence, and SA-AFT2017b transition model, $r/R = 0.76$, $M = 0.50$.

model coupled with the SA turbulence model retains the laminar behavior up to higher angles of attack. At $r/R = 0.75$, station 6 conditions are compared with laminar simulations at two Mach numbers, $M = 0.20$ (Fig. 14, “incompressible”) and $M = 0.50$ (Fig. 15, approximate Mach number for station 6 in hover).

Rumsey and Spalart [52] discuss the use of the SA turbulence model at low Reynolds numbers and note that “at low Re_c it is likely that the turbulence models will not become activated over much of the airfoil surface, and the higher the Mach number, the larger the laminar region is likely to be.”

The results at $M = 0.20$ indeed show that in the linear regime the performance of the airfoils is very similar between laminar, transition, and fully turbulent simulations.

The polar in Fig. 15 shows that turbulence model produces higher efficiency at higher Mach numbers. The sharp drop in lift-to-drag ratio of the turbulence-transition model in Fig. 15 around $c_d \approx 0.10$

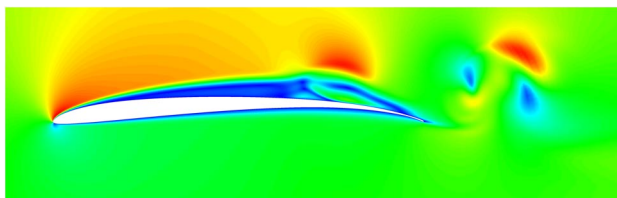


Fig. 16 Shear-layer roll-up at $r/R = 0.76$, $\alpha = 6.00^\circ$, $M = 0.50$ (velocity magnitude, time-accurate, with transition model).

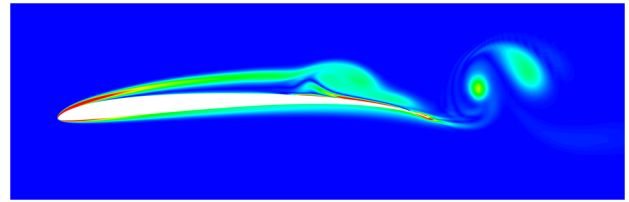


Fig. 17 Shear-layer roll-up at $r/R = 0.76$, $\alpha = 6.00^\circ$, $M = 0.50$ (vorticity magnitude, time-accurate, with transition model).

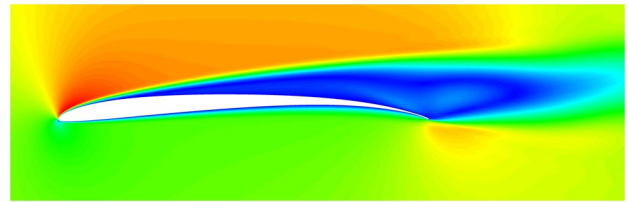


Fig. 18 Separated shear layer at $r/R = 0.76$, $\alpha = 7.00^\circ$, $M = 0.50$ (velocity magnitude, time-accurate, with transition model).

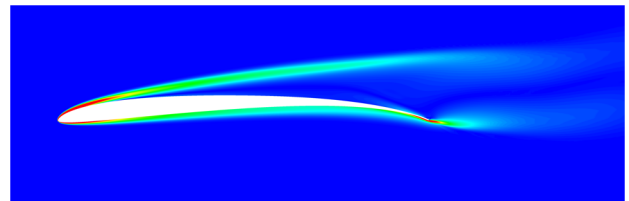


Fig. 19 Separated shear layer at $r/R = 0.76$, $\alpha = 7.00^\circ$, $M = 0.50$ (vorticity magnitude, time-accurate, with transition model).

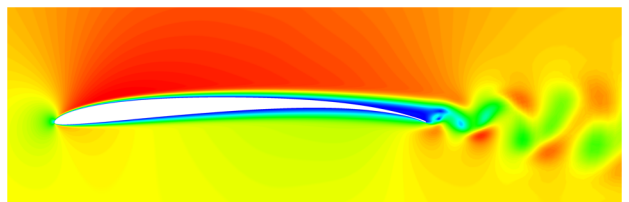


Fig. 20 Attached laminar boundary layer with separation near trailing edge at $r/R = 0.76$, $\alpha = 2.00^\circ$, $M = 0.50$ (velocity magnitude, time-accurate, with transition model).

and $c_l \approx 1.00$ is due to a simulated flow state change from a partially attached laminar BL that separates with shear-layer roll-up (Figs. 16 and 17) to a fully separated laminar shear layer without “reattachment” (Figs. 18 and 19). These correspond roughly to state D and C in Fig. 5, respectively.

The simulations in Figs. 16 and 17 perform similarly to laminar simulations. If the simulation is time averaged, the flowfield could average out to a bubble structure. Because the flow structure is similar to laminar cases, it is important to note that this would constitute a completely laminar bubble up to and including $\alpha = 6^\circ$ (flow structure D in Fig. 5).

The transition model influences the shear-layer roll-up that results in a performance decrease at around $c_d \approx 0.06$ and $c_l \approx -0.10$ when compared with the laminar cases, in which the shear layer keeps rolling up. This “stall” process is similar to that observed by Wang et al., as shown in Fig. 5 (flow structure D to C) [29].

At lower angles of attack, the laminar boundary layer stays attached over the majority of the chord length (Figs. 20 and 21), similar to flow structure B in Fig. 5.

The performance reduction on the negative lift coefficient side in Fig. 15 shows similar characteristics. Figures 22 and 23 show the different flow structures before and after the performance decrease, respectively.

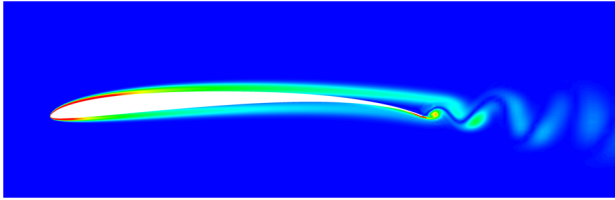


Fig. 21 Attached laminar boundary layer with separation near trailing edge at $r/R = 0.76, \alpha = 2.00^\circ, M = 0.50$ (vorticity magnitude, time-accurate, with transition model).

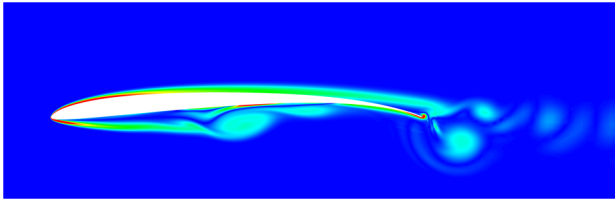


Fig. 22 Shear-layer roll-up at $r/R = 0.76, \alpha = -2.00^\circ, M = 0.50$ (vorticity magnitude, time-accurate, with transition model).

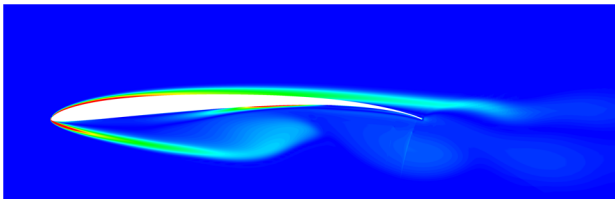


Fig. 23 Separated shear layer at $r/R = 0.76, \alpha = -3.00^\circ, M = 0.50$ (vorticity magnitude, time-accurate, with transition model).

VII. Rotor Performance

All simulations are postprocessed into C81 airfoil format. In total, four rotor models are generated, two for JPL SS conditions and two for MC 2 conditions, one using the SA turbulence model and the other using the AFT2017b transition model.

The coaxial rotor performance was calculated using CAMRAD II, a comprehensive analysis tool for rotorcraft [53]. CAMRAD II has undergone extensive correlation of performance and loads measurements on rotorcraft, including coaxial rotors [54]. The CAMRAD II aerodynamic model for the rotor blade is based on lifting-line theory, using steady two-dimensional airfoil characteristics and a vortex wake model, plus models for unsteady flow (attached flow and dynamic stall) and yawed/swept flow. Effects of compressibility (Mach numbers) and viscosity (Reynolds number, stall, and drag) enter through airfoil table data: lift, drag, and moment coefficients of two-dimensional sections as function of angle of attack and Mach number, for the appropriate chord and atmosphere (density, temperature) so as to have correct Reynolds number variation with Mach number. The vortex wake consists of rolled-up tip vortices and inboard vortex sheets, emanating from each blade. Second-order lifting-line theory gives the vortex-induced loading on the blades well. Free wake geometry calculations give the self-induced distortion of the intertwined, interacting tip vortices, including the mutual interaction of the wake from the two coaxial rotors. The CAMRAD II blade structural model is based on nonlinear beam theory of rotating finite elements.

A. Rotor Performance Correlation to JPL Test Data

The MH test data are obtained under simulated Mars atmospheric conditions in the JPL 25-ft-diam Space Simulator. The chamber was evacuated to vacuum and backfilled with CO_2 gas to a density of $\rho = 0.0175 \text{ kg/m}^3$, whereas the temperature was kept at ambient conditions, $T = 20^\circ\text{C}$. The helicopter was operated with a conservative tip speed of $M_{\text{tip}} = 0.62$ at 2600 RPM, resulting in a thrust of up to $T = 13.25 \text{ N}$. Several items, such as the power source, were connected from the ground through an electrical tether to reduce

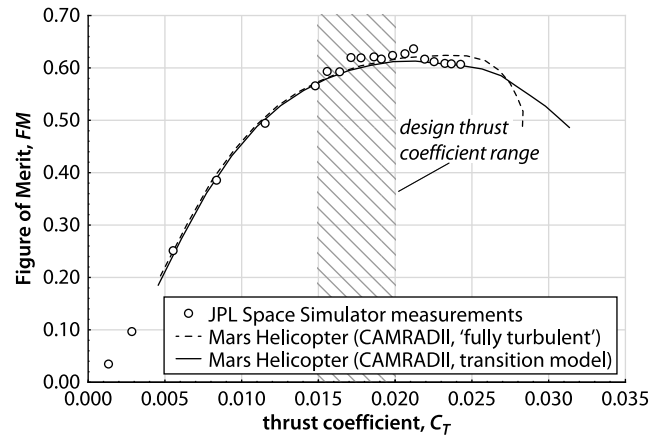


Fig. 24 Figure of merit versus thrust for $\rho = 0.0175 \text{ kg/m}^3$ and $T = 20^\circ\text{C}$ (JPL SS test conditions), including JPL 25-ft-diam Space Simulator measurements.

the mass of the vehicle in order to account for the difference in gravity between Earth and Mars. More details on the test setup can be found in the work by Balaram et al. [1]. Figure 24 shows rotor model performance predictions in terms of the FM versus thrust coefficient for JPL SS conditions.

Both rotor models are generated for JPL SS conditions and perform similarly up to around $C_T = 0.018$. Beyond this point the rotor models with the transition model start predicting lower efficiencies over the design thrust coefficient range.

Apart from the outliers, the transition model curve matches the performance predictions well, even after peak FM thrust. Figure 25 shows the same data points but expressed as power versus thrust curves.

Both performance comparisons show good agreement in the design thrust coefficient range of the MH. Modeling of stall is difficult but seems to be reasonably captured in the transition model, whereas the turbulence model by itself produces an overestimate of the efficiency metric, but a reduction of maximum thrust.

B. Rotor Performance Predictions in the Martian Atmosphere

Figure 26 shows the FM versus thrust coefficient for rotor models generated for MC 2 conditions.

The FM is slightly increased for MC 2 conditions relative to JPL SS conditions in the design thrust coefficient range. This is most likely a direct effect of Mach number and Reynolds number differences due to the difference in temperature between the JPL SS and MC 2 conditions, resulting in a conservative estimate obtained

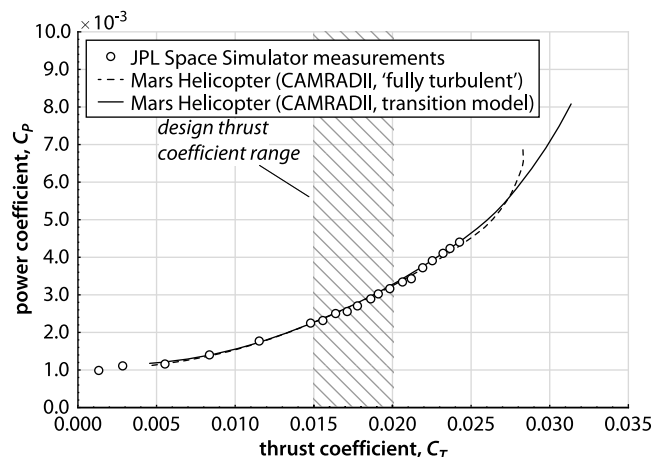


Fig. 25 Thrust versus power for $\rho = 0.0175 \text{ kg/m}^3$ and $T = 20^\circ\text{C}$ (JPL SS test conditions), including JPL 25-ft-diam Space Simulator measurements.

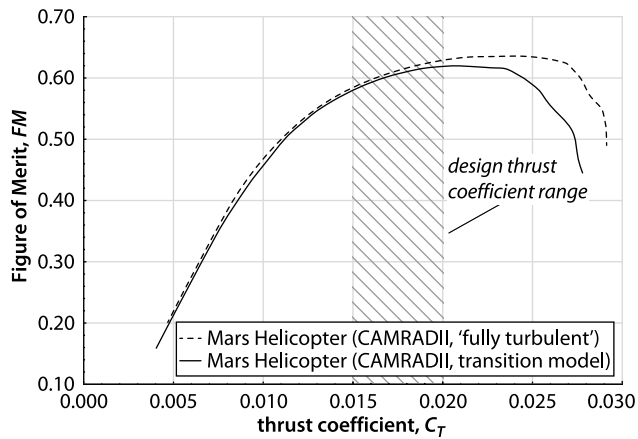


Fig. 26 Figure of merit versus thrust for $\rho = 0.017 \text{ kg/m}^3$ and $T = -50^\circ\text{C}$ (Mars condition 2).

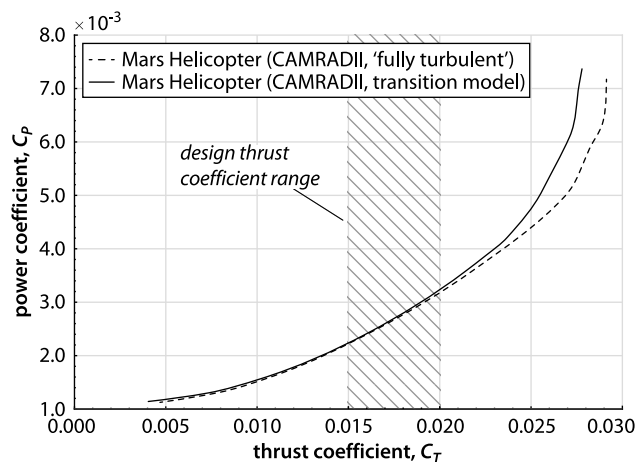


Fig. 27 Thrust versus power for $\rho = 0.017 \text{ kg/m}^3$ and $T = -50^\circ\text{C}$ (Mars condition 2).

from the experiments. Figure 27 shows power versus thrust curves for the two rotor models in MC 2 conditions.

The reason for the difference in characteristic shape of the FM curve for the transition model between JPL SS and MC 2 conditions is no doubt related to different predictions of stall characteristics and deserves further investigation.

VIII. Conclusions

For both Jet Propulsion Laboratory (JPL) SS and MC 2 conditions, the rotor model with a transition model and with a “fully turbulent” model perform similarly over the design thrust coefficient range. At higher collective settings the transition model predicts lower efficiencies, attributed to the absence of transition modeling in the fully turbulent model. This results in earlier separation and reduced performance. The transition-model-based rotor model shows good agreement with the JPL test data over the entire thrust coefficient range. The rotor figure of merit is shown to be 1.3–2.6% higher over the design thrust coefficient range for MC 2, compared with experimental measurements. This implies a slight thrust margin over JPL measured performance when taking the transition-based model as the conservative predictor of estimated performance.

Using the transition model, the flow structures observed around the airfoils resemble the low-Reynolds-number structures observed in experiments. At low angles of attack the laminar boundary layer is partially attached and could experience laminar-turbulent transition downstream, depending on the Reynolds numbers and external factors. With increasing angle of attack the separation location on the upper surface will move toward the leading edge, causing the laminar shear layer to “roll-up,” without large consequences to the airfoil

performance. Further increasing the angle of attack will cause the shear layer to fail to “reattach,” deteriorating the airfoil’s performance.

Future work: The sensitivity of airfoil performance to freestream turbulence intensity (and its distribution across the frequency spectrum), vibrations, surface roughness, and dust needs to be evaluated for this Reynolds number range. Furthermore, differences between the two-dimensional and three-dimensional flow fields need to be investigated to ensure that no first-order flow physics are overlooked using a comprehensive analyses approach for performance estimations of the Mars Helicopter.

Acknowledgments

The authors would like to thank Ethan Romander, Mark Potsdam, Pieter Buning, Natasha Schatzman, and Belen Veras-Alba for their insights for the OVERFLOW simulations and assistance with running the cases. The research of Håvard F. Grip was carried out at the Jet Propulsion Laboratory, California Institute of Technology, under a contract with the National Aeronautics and Space Administration. Eduardo Solis and Patricia Ventura-Diaz are thanked for their assistance in preparing the airfoil geometry and mesh. Jason Cornelius, Haley Cummings, Kristen Kallstrom, Keiko Nagami, Brenda Natalia Perez Perez, Ethan Romander, Alan Wadcock, and Larry Young provided invaluable feedback on this paper. The support from William Warmbrodt and Stephen Lesh during this research is greatly appreciated.

References

- [1] Balam, J., and Tokumaru, P. T., “Rotorcrafts for Mars Exploration,” *11th International Planetary Probe Workshop*, Pasadena, CA, 2014, <https://www.hou.usra.edu/meetings/ippw2014/>, <https://publib.jpl.nasa.gov/docushare/dsweb/Services/Document-3749>.
- [2] Grip, H. F., Johnson, W., Malpica, C., Scharf, D. P., Mandić, M., Young, L., Allan, B., Mettler, B., and Martin, M. S., “Flight Dynamics of a Mars Helicopter,” *43rd European Rotorcraft Forum*, Council of European Aerospace Societies (CEAS), Milan, 2017, <https://rotorcraft-forum.eu/about-us/the-erf/>.
- [3] Balam, J. (Bob), Canham, T., Duncan, C., Golombek, M., Grip, H. F., Johnson, W., Maki, J., Quon, A., Stern, R., and Zhu, D., “Mars Helicopter Technology Demonstrator,” *AIAA Science and Technology Forum and Exposition (AIAA SciTech)*, AIAA Paper 2018-0023, 2018. doi:10.2514/6.2018-0023
- [4] Koning, W. J. F., Johnson, W., and Allan, B. G., “Generation of Mars Helicopter Rotor Model for Comprehensive Analyses,” *AHS Aeromechanics Design for Transformative Vertical Flight*, American Helicopter Soc. (AHS) SKU#: sm_aeromech_2018_17, Fairfax, VA, 2018, <https://vtol.org/store/product/generation-of-mars-helicopter-rotor-model-for-comprehensive-analyses-12573.cfm>.
- [5] Koning, W. J. F., Romander, E. A., and Johnson, W., “Low Reynolds Number Airfoil Evaluation for the Mars Helicopter Rotor,” *AHS International 74th Annual Forum & Technology Display*, American Helicopter Soc. (AHS) SKU#: 74-2018-0169, Fairfax, VA, 2018, <https://vtol.org/store/product/low-reynolds-number-airfoil-evaluation-for-the-mars-helicopter-rotor-12679.cfm>.
- [6] Jet Propulsion Laboratory, “Helicopter Could Be ‘Scout’ for Mars Rovers,” 2015, <https://www.jpl.nasa.gov/news/news.php?feature=4457> [accessed 12 June 2017].
- [7] Young, L. A., Aiken, E. W., Derby, M., Demblewski, R., and Navarrete, J., “Experimental Investigation and Demonstration of Rotary-Wing Technologies for Flight in the Atmosphere of Mars,” *AHS International 58th Annual Forum & Technology Display*, American Helicopter Soc. (AHS) SKU#: 58-2002-00064, Fairfax, VA, 2002, <https://vtol.org/store/product/experimental-investigation-and-demonstration-of-rotarywing-technologies-for-flight-in-the-atmosphere-of-mars-2170.cfm>.
- [8] Young, L. A., Aiken, E., Lee, P., and Briggs, G., “Mars Rotorcraft: Possibilities, Limitations, and Implications for Human/Robotic Exploration,” *IEEE Aerospace Conference*, Inst. of Electrical and Electronics Engineers (IEEE) Aerospace, New York, 2005, <https://ieeexplore.ieee.org/document/1559324>. doi:10.1109/AERO.2005.1559324
- [9] Young, L., Aiken, E., Johnson, J., Demblewski, R., Andrews, J., and Klem, J., “New Concepts and Perspectives on Micro-Rotorcraft and Small Autonomous Rotary-Wing Vehicles,” *20th AIAA Applied*

- Aerodynamics Conference*, AIAA Paper 2002-2816, 2002.
doi:10.2514/6.2002-2816
- [10] Escobar, D., Chopra, I., and Datta, A., "Aeromechanical Loads on a Mars Coaxial Rotor," *AHS International 74th Annual Forum & Technology Display*, American Helicopter Soc. (AHS) SKU#: 74-2018-1268, Phoenix, AZ, 2018, <https://vtol.org/store/product/aeromechanical-loads-on-a-mars-coaxial-rotor-12751.cfm>.
 - [11] Hoerner, S. F., *Fluid-Dynamic Drag: Practical Information on Aerodynamic Drag and Hydrodynamic Resistance*, Hoerner Fluid Dynamics, Bricktown, NJ, 1965, Chaps. 3, 5, 6, 15, 19.
 - [12] McMasters, J., and Henderson, M., "Low-Speed Single-Element Airfoil Synthesis," *Technical Soaring*, Vol. 6, No. 2, 1980, pp. 1–21.
 - [13] Schlichting, H., and Kestin, J., *Boundary-Layer Theory*, 7th ed., McGraw-Hill, New York, 1979, Chaps. 2, 7, 10, 13, 16, 17.
 - [14] Wazzan, A. R., Okamura, T. T., and Smith, A. M. O., "Spatial and Temporal Stability Charts for the Falkner-Skan Boundary-Layer Profiles," McDonnell Douglas TR DAC-67086, Santa Monica, CA, 1968.
 - [15] Drela, M., "XFOIL: An Analysis and Design System for Low Reynolds Number Airfoils," *Low Reynolds Number Aerodynamics*, edited by T. J. Mueller, Vol. 54, Lecture Notes in Engineering, Springer, Berlin, pp. 1–12.
doi:10.1007/978-3-642-84010-4_1
 - [16] Smith, A. M. O., and Gamberoni, N., "Transition, Pressure Gradient, and Stability Theory," Douglas Aircraft Division TR ES 26388, El Segundo, CA, 1956.
 - [17] van Ingen, J. L., "A Suggested Semi-Empirical Method for the Calculation of the Boundary Layer Transition Region," *Vliegtuigbouwkunde*, Technische Hogeschool Delft, Rapport VTH-74, Delft, The Netherlands, 1956.
 - [18] van Ingen, J. L., "The e^N Method for Transition Prediction. Historical Review of Work at TU Delft," *38th Fluid Dynamics Conference and Exhibit*, AIAA Paper 2008-3830, 2008.
doi:10.2514/6.2008-3830
 - [19] Lissaman, P. B. S., "Low-Reynolds-Number Airfoils," *Annual Review of Fluid Mechanics*, Vol. 15, Jan. 1983, pp. 223–239.
doi:10.1146/annurev.fl.15.010183.001255
 - [20] Mueller, T. J., and DeLaurier, J. D., "Aerodynamics of Small Vehicles," *Annual Review of Fluid Mechanics*, Vol. 35, Jan. 2003, pp. 89–111.
doi:10.1146/annurev.fluid.35.101101.161102
 - [21] Carmichael, B. H., "Low Reynolds Number Airfoil Survey, Volume 1," NASA CR-165803-VOL-1, 1981.
 - [22] Drela, M., "Higher-Order Boundary Layer Formulation and Application to Low Reynolds Number Flows," *Fixed and Flapping Wing Aerodynamics for Micro Air Vehicle Applications*, edited by T. J. Mueller, Progress in Astronautics and Aeronautics, AIAA, Washington, D.C., 2001, pp. 13–33.
doi:10.2514/5.9781600866654.0013.0033
 - [23] Alam, M. M., Zhou, Y., Yang, H. X., Guo, H., and Mi, J., "The Ultra-Low Reynolds Number Airfoil Wake," *Experiments in Fluids*, Vol. 48, Jan. 2010, pp. 81–103.
doi:10.1007/s00348-009-0713-7
 - [24] Arena, A. V., and Mueller, T. J., "Laminar Separation, Transition, and Turbulent Reattachment near the Leading Edge of Airfoils," *AIAA Journal*, Vol. 18, No. 7, 1980, pp. 747–753.
doi:10.2514/3.50815
 - [25] Crompton, M. J., "The Thin Aerofoil Leading Edge Separation Bubble," Ph.D. Dissertation, School of Civil, Aerospace and Mechanical Engineering, Univ. of Bristol, Bristol, England, 2001.
 - [26] Gaster, M., "The Structure and Behaviour of Laminar Separation Bubbles," HM Stationery Office R&M 3595, London, 1969.
 - [27] Laitone, E. V., "Wind Tunnel Tests of Wings at Reynolds Numbers Below 70 000," *Experiments in Fluids*, Vol. 23, Nov. 1997, pp. 405–409.
doi:10.1007/s003480050128
 - [28] Mueller, T. J., and Batil, S. M., "Experimental Studies of Separation on a Two-Dimensional Airfoil at Low Reynolds Numbers," *AIAA Journal*, Vol. 20, No. 4, 1982, pp. 457–463.
doi:10.2514/3.51095
 - [29] Wang, S., Zhou, Y., Alam, M. M., and Yang, H., "Turbulent Intensity and Reynolds Number Effects on an Airfoil at Low Reynolds Numbers," *Physics of Fluids*, Vol. 26, Nov. 2014, Paper 115107.
doi:10.1063/1.4901969
 - [30] Huang, R. F., and Lin, C. L., "Vortex Shedding and Shear-Layer Instability of Wing at Low-Reynolds Numbers," *AIAA Journal*, Vol. 33, No. 8, 1995, pp. 1398–1403.
doi:10.2514/3.12561
 - [31] Obert, E., *Aerodynamic Design of Transport Aircraft*, IOS Press, Amsterdam, 2009, pp. 119–123.
 - [32] Broeren, A. P., and Bragg, M. B., "Unsteady Stalling Characteristics of Thin Airfoils at Low Reynolds Number," *Fixed and Flapping Wing Aerodynamics for Micro Air Vehicle Applications*, edited by T. J. Mueller, Progress in Astronautics and Aeronautics, AIAA, Washington, D.C., 2001, pp. 191–213.
doi:10.2514/5.9781600866654.0191.0213
 - [33] Yarusyevych, S., Sullivan, P. E., and Kawall, J. G., "On Vortex Shedding from an Airfoil in Low-Reynolds-Number Flows," *Journal of Fluid Mechanics*, Vol. 632, Aug. 2009, pp. 245–271.
doi:10.1017/S0022112009007058
 - [34] Sunada, S., Sakaguchi, A., and Kawachi, K., "Airfoil Section Characteristics at a Low Reynolds Number," *Journal of Fluids Engineering*, Vol. 119, March 1997, pp. 129–135.
doi:10.1115/1.2819098
 - [35] Okamoto, M., Yasuda, K., and Azuma, A., "Aerodynamic Characteristics of the Wings and Body of a Dragonfly," *The Journal of Experimental Biology*, Vol. 199, No. 2, 1996, pp. 281–294.
 - [36] Schmitz, F. W., "Aerodynamics of the Model Airplane. Part 1—Airfoil Measurements," NASA TM-X-60976, 1967.
 - [37] Pelletier, A., and Mueller, T. J., "Low Reynolds Number Aerodynamics of Low-Aspect-Ratio, Thin/Flat/Cambered-Plate Wings," *Journal of Aircraft*, Vol. 37, No. 5, 2000, pp. 825–832.
doi:10.2514/2.2676
 - [38] Werlé, H., *Le tunnel hydrodynamique au service de la recherche aérospatiale*, Office National d'Études et de Recherches Aérospatiales, Chatillon, France, 1974, pp. 42–43.
 - [39] Van Dyke, M., *An Album of Fluid Motion*, The Parabolic Press, Stanford, CA, 1982, pp. 24–26.
 - [40] Suwa, T., Nose, K., Numata, D., Nagai, H., and Asai, K., "Compressibility Effects on Airfoil Aerodynamics at Low Reynolds Number," *30th AIAA Applied Aerodynamics Conference*, AIAA Paper 2012-3029, 2012.
doi:10.2514/6.2012-3029
 - [41] Anyoji, M., Numata, D., Nagai, H., and Asai, K., "Effects of Mach Number and Specific Heat Ratio on Low-Reynolds-Number Airfoil Flows," *AIAA Journal*, Vol. 53, No. 6, 2014, pp. 1640–1654.
doi:10.2514/1.J053468
 - [42] Anyoji, M., Nonomura, T., Aono, H., Oyama, A., Fujii, K., Nagai, H., and Asai, K., "Computational and Experimental Analysis of a High-Performance Airfoil Under Low-Reynolds-Number Flow Condition," *Journal of Aircraft*, Vol. 51, No. 6, 2014, pp. 1864–1872.
doi:10.2514/1.C032553
 - [43] Sampaio, L. E. B., Rezende, A. L. T., and Nieckele, A. O., "The Challenging Case of the Turbulent Flow Around a Thin Plate Wing Deflector, and its Numerical Prediction by LES and RANS Models," *Journal of Wind Engineering and Industrial Aerodynamics*, Vol. 133, Oct. 2014, pp. 52–64.
doi:10.1016/j.jweia.2014.07.007
 - [44] Pauley, L. L., Moin, P., and Reynolds, W. C., "The Structure of Two-Dimensional Separation," *Journal of Fluid Mechanics*, Vol. 220, Nov. 1990, pp. 397–411.
doi:10.1017/S0022112090003317
 - [45] Buning, P., and Nichols, R., *User's Manual for OVERFLOW 2.2*, NASA Langley Research Center, Hampton, VA, 2008.
 - [46] Pulliam, T., "High Order Accurate Finite-Difference Methods: As Seen in OVERFLOW," *20th AIAA Computational Fluid Dynamics Conference*, AIAA Paper 2011-3851, June 2011.
doi:10.2514/6.2011-3851
 - [47] Spalart, P. R., and Allmaras, S. R., "A One-Equation Turbulence Model for Aerodynamic Flows," *30th Aerospace Sciences Meeting & Exhibit*, AIAA Paper 1992-439, 1992.
doi:10.2514/6.1992-439
 - [48] Coder, J. G., and Maughmer, M. D., "Computational Fluid Dynamics Compatible Transition Modeling Using an Amplification Factor Transport Equation," *AIAA Journal*, Vol. 52, No. 11, 2014, pp. 2506–2512.
doi:10.2514/1.J052905
 - [49] Rumsey, C. L., Slotnick, J. P., and Sclafani, A. J., "Overview and Summary of the Third AIAA High Lift Prediction Workshop," *2018 AIAA Aerospace Sciences Meeting*, AIAA Paper 2018-1258, 2018.
doi:10.2514/6.2018-1258
 - [50] Chan, W. M., Rogers, S. E., Nash, S. M., Buning, P. G., Meakin, R. L., Boger, D. A., and Pandya, S., *Chimera Grid Tools User's Manual, Version 2.0*, NASA Ames Research Center, Hampton, VA, 2007.
 - [51] Munday, P. M., Taira, K., Suwa, T., Numata, D., and Asai, K., "Nonlinear Lift on a Triangular Airfoil in Low-Reynolds-Number Compressible Flow," *Journal of Aircraft*, Vol. 52, No. 3, 2015, pp. 924–931.
doi:10.2514/1.C032983

- [52] Rumsey, C. L., and Spalart, P. R., "Turbulence Model Behavior in Low Reynolds Number Regions of Aerodynamic Flowfields," *AIAA Journal*, Vol. 47, No. 4, 2009, pp. 982–993.
doi:10.2514/1.39947
- [53] Johnson, W., "Rotorcraft Aerodynamics Models for a Comprehensive Analysis," *AHS International 54th Annual Forum & Technology Display*, American Helicopter Soc. SKU#: 54-00103, Fairfax, VA, 1998, <https://vtol.org/store/product/rotorcraft-aerodynamics-models-for-a-comprehensive-analysis-4591.cfm>.
- [54] Johnson, W., "Influence of Lift Offset on Rotorcraft Performance," NASA TP-2009-215404, 2009.

M. Smith
Associate Editor